JOURNAL OF MATERIALS SCIENCE 25 (1990) 5043–5054

Thermal fatigue in polycrystalline alumina

W. J. LEE, E. D. CASE
Department of Metallurgy Mechanics and Materials Science, Michigan State University, East Lansing, Michigan 48824, USA

Damage accumulation in polycrystalline alumina subjected to cyclic thermal loading was studied via non-destructive elastic modulus and internal friction measurements. These non-destructive techniques were sensitive to cracks formed by thermal loading. Thermal shock damage was observed to saturate as a function of an increasing cumulative number of thermal shock cycles. The observed power law relationship between the damage saturation and thermal shock difference implies a fatigue-like power law relation in stress. The exponent has a value of approximately 12 for the range of ΔT included in this study. Thermal shock damage induced changes in internal friction were found to be a function of a crack damage parameter. These thermal fatigue results of polycrystalline (unreinforced) alumina are also compared to thermal fatigue results for SiC whisker–alumina composites.

1. Introduction

Thermal shock damage may result from any rapid temperature change which induces large thermal stresses in a component. Gas turbine components, high temperature valves, and heat engine components and other criticial applications of ceramics often involve thermal fatigue, hence a detailed investigation of cyclic thermal shock is necessary.

A number of difficulties are encountered in fatigue testing of brittle materials. In order to characterize the strength of brittle ceramic materials, a large number of test specimens is required [1–3]. Scatter in strength data may sometimes obscure the fundamental trends in the data [1–3]. Non-destructive techniques such as elasticity and internal friction can measure changes induced by thermal shock damage [4–9]. In addition, the crack-induced changes in the elasticity and internal friction reflect the entire flaw population [9], whereas the strength changes can be attributed to changes in the critical flaw lengths.

The present study compares cyclic thermal shock damage in polycrystalline alumina to results of a previous thermal fatigue on alumina–SiC whisker reinforced ceramic–ceramic composites [5]. In both studies, the evolving crack damage was monitored non-destructively via elastic modulus and internal friction measurements.

1.1. Fatigue in ceramics – Literature review

Recent work [10–14] has shown that crack extension due to repeated mechanical loading of ceramics can be described in equations that are similar in form to those developed for fatigue crack propagation in metals [15], namely

$$da/dn = W\Delta K^q \quad (1)$$

where a is the length of the fatigue crack, n the cumulative number of stress cycles, ΔK the stress intensity range $K_{max} - K_{min}$, and the parameters W and q depend on the material, the test temperature, etc.

Table I summarizes the materials, test geometries, crack propagation rates, and proposed energy dissipation mechanisms for studies of repeated mechanical loading of ceramics. The authors in each of these studies (Table I) expressed their crack propagation data in terms of Equation 1 (except in [11], as noted in Table I). Note that while experimentally determined values of the fatigue exponent, q, for metals typically range from about 2 to 7 [15], q ranges from about 9 to 27 for the ceramic materials included in Table I.

Several researchers have noted effects such as fatigue crack closure and crack branching in ceramics under repeated mechanical loading. Dauskardt *et al.* [13] measure fatigue crack closure in stabilized zirconia using a strain gauge. Magnesia stabilized zirconia compact tension specimens showed evidence of fatigue crack closure behaviour similar to that observed in metals [13]. Dauskardt *et al.* [13] suggested that the fatigue in these toughened ceramics may be related to several mechanisms including crack tip shielding by stress induced phase transformation [16, 17], crack deflection [18, 19], crack bridging [20] and crack surface asperity wedging [21–27]. Optical micrographs of the crack path support the crack deflection and crack bridging hypothesis [13].

Kim and Mubeen [14] attribute the fatigue in Westerly granite to the crack closure due to crack face interference [21–27] and crack branching [28]. SEM micrographs of replicas taken from the near-notch area in the granite specimens [14] indicate crack branching along the grain boundaries. From the morphology of the observed cracks, Kim and Mubeen assumed that the crack arrested at several points. The repeated crack arrest was assumed to correspond to a temporary reduction in da/dn, where da/dn was inferred from compliance measurements.

Under cyclic compression loading, Suresh and coworkers observed stable crack growth for pre-notched specimens of unreinforced polycrystalline alumina [21–24], SiC whisker reinfored Si_3N_4 [25], and

0022–2461/90 $03.00 + .12

SiC whisker reinforced alumina [26]. For each material, the macrocrack propagating from the pre-notch was monitored (on both sides of the specimen) by a travelling optical microscope. The macrocrack growth rates decreased monotonically as the crack length increased. A graph of crack length plotted against the cumulative number of load cycles showed a series of plateaux which may indicate steady state behaviour over certain intervals of cyclic loading. The plateaus in crack length during cyclic loading, as observed by Suresh, perhaps may be similar to the crack damage saturation behaviour observed in thermally fatigued monolithic polycrystalline alumina (present study) and in SiC whisker reinforced alumina [5].

Suresh and coworkers explained the fatigue crack growth by a combination of several plausible physical mechanisms. Unreinforced ceramics, ceramic–metal composites, and ceramic–ceramic composites may involve different mechanisms, at least in part due to differing microstructures. For unreinforced ceramics, such as the polycrystalline alumina in Suresh's study [21–24] and the polycrystalline alumina in the present study, the possible mechanisms for the fatigue crack growth include crack wedging by crack debris [10], tensile residual stress at the notch tip [21], frictional sliding and opening of microcrack [28], and grain boundary cracking induced by compressive loads and residual thermal stresses [29].

The experimental observations of Reece [10], Grossmuller [12], Hoshide [11], Dauskardt [13], Kim and Mubeen [14], and Suresh [21–27] indicate the presence of fatigue effects in toughened ceramics [12, 13], polycrystalline ceramics [10, 11, 22–24], geological materials [14], and ceramic–ceramic composites [25, 26] under cyclic mechanical loading. In addition to involving purely mechanical loading, the cyclic mechanical loading research cited above involves measurements on a single advancing macrocrack, although microcracks may be generated in the vicinity of the macrocrack. The thermal shock loading studies of unreinforced alumina (this study) and SiC whisker reinforced alumina [4, 5] by the present authors involve "distributed" damage, in that it is no longer limited to a single advancing crack.

2. Experimental procedure

2.1. Materials

Alumina substrates (96% alumina) used for this research were supplied by Saxonburg Ceramic Incorporated (Monroe, NC). The as-received specimens were rectangular plates with dimensions of 11.5 × 11.5 × 0.1 cm^3. Specimens were cut into prismatic bars using a low speed diamond saw. The edges of cut specimens were polished using 600 grit SiC paper to obtain a more uniform width, however, the specimens were not intentionally edge bevelled. Then the specimens were annealed in air at 1150° C for 12 h to remove residual stresses that may have been present due to processing or due to specimen preparation. The dimensions of annealed specimens are given in Table II . An average grain size of 10 μm was determined by the linear intercept technique on SEM micrographs on fracture surfaces (Fig. 1). The average grain size was computed by multiplying the average intercept length by a correction factor of 1.5 [30]. The mass density of the polycrystalline alumina used in this study, as determined from the mass and dimensions of each specimen, ranged from 3.68 to 3.74 g cm^{-3}. This corresponds to a volume fraction porosity of approximately 6 to 7.4%.

Since the comparison of the thermal shock damage results for the unreinforced polycrystalline alumina and the SiC whisker reinforced alumina will be central to this paper, the material properties of the SiC whisker–alumina composites will be reviewed here, with additional details available in [5]. Whisker

TABLE I Survey of fatigue crack behaviour for ceramics subjected to cyclic mechanical loading

Test specimen (material and geometry)	da/dN range (m/cycle)	Fatigue exponent q	Proposed dissipation mechanism	Starting flaws	Reference
1. Alumina					
a. Wedge opening loaded	10^{-9}–10^{-7}	14	Wedging and sliding asperity	Notch	[10]
b. Tapered double cantilever beam	10^{-9}–10^{-6}	27	Wedging and sliding asperity	Notch	[10]
c. Three-point bend‡	10^{-8}–10^{-5}	9.12	*	Indentation flaws	[11]
2. MgO-PSZ					
a. Compressive loading	10^{-9}–10^{-7}	13†	*	Hole	[12]
b. Compact-tension (specimens loaded in tension-tension)	10^{-10}–10^{-6}	24	Transformation, crack closure, crack deflection and crack bridging	Notch	[13]
3. Silicon nitride					
a. Three-point bend‡	10^{-10}–10^{-6}	21.1	*	Indentation flaws	[11]
4. Westerly granite					
a. Three-point bend	10^{-10}–10^{-8}	12	Crack closure and crack branching	Slot	[14]

*Dissipation mechanisms were not proposed for this study.
†Fatigue exponent calculated by the present authors from da/dn against K plot of Grossmuller [12].
‡The authors in this study expressed their crack propagation rate in terms of K_{eff} instead of ΔK.

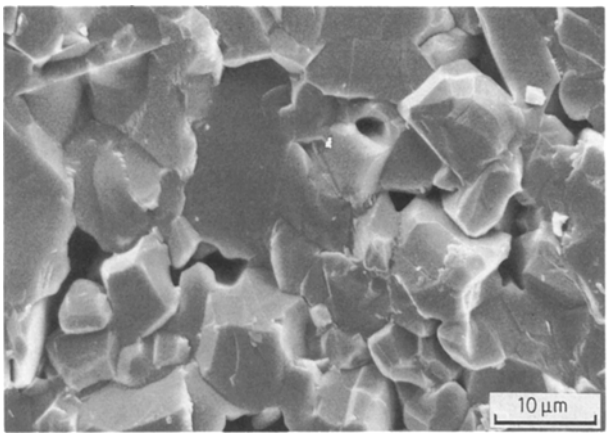

Figure 1 A SEM micrograph showing a fracture surface of the polycrystalline alumina specimens.

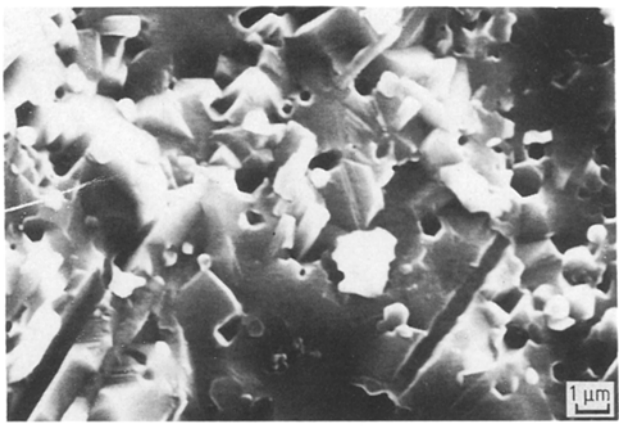

Figure 2 A fracture surface of a SiC whisker reinforced alumina specimen [5].

reinforced alumina composites were processed by Alcoa from A-16 SG alumina, reinforced with 20 vol % of SiC whiskers. Dimensions of the as-received specimens were $7 \times 0.7 \times 0.3\,cm^3$. Mass density of the specimens ranged from 3.76 to $3.80\,g\,cm^{-3}$. The average grain size of the alumina matrix was approximately 4 to $6\,\mu m$, as determined by linear intercept technique on SEM micrographs of fracture surfaces, again computing the average grain size by multiplying the average intercept length by 1.5 [30]. A SEM micrograph of a fracture surface of the SiC whisker reinforced alumina composite is given in Fig. 2.

2.2. Elasticity and internal friction measurements

The elasticity and internal friction measurements were made by the sonic resonance technique [31]. A block diagram for the modulus and internal friction equipment is shown in Fig. 3. The flexural and the torsional resonant frequencies data were converted into Young's and shear moduli values by using the equations of Pickett [32] and the modification given by Hasselman [33]. Equation 2 was used to compute Poisson's ratio, v, from the measured Young's modulus, E, and shear modulus, G,

$$v = E/2G - 1 \quad (2)$$

The internal friction was determined by the free decay method [34], in which the specimen is driven at a mechanical resonance, then the driving signal is turned off and the number of cycles, S, required for the signal amplitude to decay from amplitude I_1 to amplitude I_2 is measured electronically (Fig. 4). The measured internal friction, Q^{-1}, is given by

$$Q^{-1} = \ln (I_1/I_2)/\pi S \quad (3)$$

The measured internal friction represents two damping contributions: (1) Q_s^{-1}, the internal friction due to the specimen itself and (2) Q_a^{-1}, the internal friction due to the apparatus. The specimen and apparatus contributions may be separated by measuring internal friction as a function of suspension position [34]. All internal friction values reported in this paper are those for specimen internal friction only. Details of the apparatus and the internal friction measurement procedure are given elsewhere [4–6].

TABLE II Dimensions, mass, and mass density of alumina specimens

Specimen label	Dimensions (cm)	Mass (g)	Density ($g\,cm^{-3}$)
A1	11.48 × 1.23 × 0.108	5.6741	3.720
A2	11.45 × 1.27 × 0.108	5.8513	3.716
A3	11.39 × 1.28 × 0.108	5.7738	3.683
A4	11.47 × 1.28 × 0.107	5.8162	3.715
A5	11.48 × 1.26 × 0.108	5.8148	3.737
A6	11.49 × 1.24 × 0.108	5.7210	3.727

2.3. Cyclic thermal shock test

Cyclic thermal shock tests were performed using the apparatus shown in Fig. 5. Details of the apparatus are given elsewhere [4]. Thermal shock specimens were held at a preselected temperature for 20 mins in a vertical-muffle electric furnace before quenching into a container of distilled water. The temperature of the water bath was approximately 21° C and was measured by a mercury-in-glass thermometer. After the specimens had been subjected to a preselected cumulative number of thermal shock cycles, the elastic modulus and internal friction were measured for each specimen. The observed changes in the elastic modulus and internal friction as a function of thermal shock treatment were used to assess the accumulated thermal shock-induced damage.

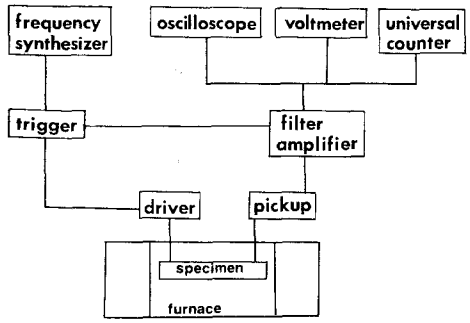

Figure 3 Schematic of the sonic resonance apparatus for determining the elastic moduli and the apparatus for determining internal friction via the log decrement method (free decay of the natural vibration modes).

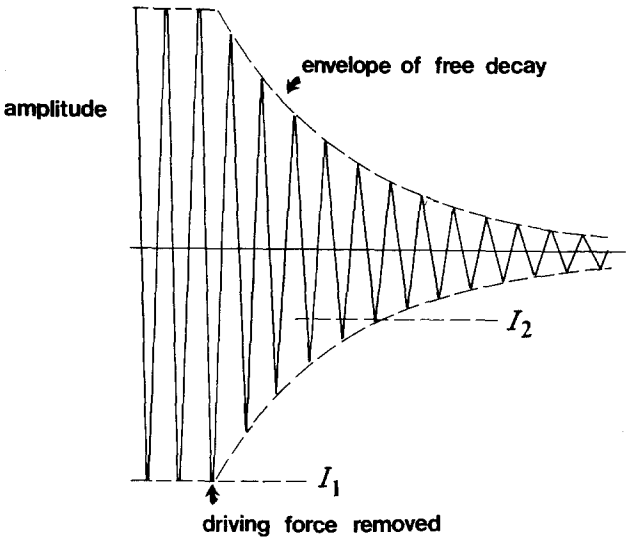

Figure 4 Free decay of natural vibration of an anelastic solid, which is the basis for the internal friction measurements.

3. Results and discussion

3.1. Young's modulus, shear modulus and internal friction of unshocked specimens

The initial (unshocked) values of Young's modulus, shear modulus, internal friction, and Poisson's ratio are listed in Table III for each of the specimens included in this study. As is typical for polycrystalline ceramics [35–39], the Young's modulus and shear modulus of all the unshocked specimens decreased with increasing porosity. The unreinforced alumina specimens exhibit a relatively limited range of porosity, which in turn implies limited effects due to porosity. Appendix A includes a discussion of modulus and internal friction dependencies on porosity.

For unshocked specimens of unreinforced alumina, the internal friction of alumina varied from 6.23 to 10.6 $\times$ 10^{-5}, while that of unshocked SiC whisker reinforced alumina [5] ranged from 13.2 to 18.6 $\times$ 10^{-5}. The internal friction values of the unreinforced alumina were thus about 50% lower than those of SiC whisker reinforced composites, despite the fact that elastic moduli for the composite were about 20% higher than those of the unreinforced alumina. The higher internal friction of the composites might be explained on the basis of the residual stresses [5, 6] and the presence of interfaces between the matrix and the whiskers†, but further work needs to be done to clarify such differences in the internal friction for the composite and non-composite specimens.

TABLE III Room temperature Young's modulus (E), shear modulus (G), Poisson's ratio (v) and internal friction (Q) for unshocked unreinforced alumina specimens (after annealing)

Specimen	E (GPa)	G (GPa)	v	Q^{-1} ($\times 10^{-5}$)
A1	333.85	135.68	0.23	10.6
A2	332.96	135.17	0.22	8.1
A3	323.87	132.78	0.23	8.57
A4	332.5	135.32	0.23	8.3
A5	338.53	*	*	6.23
A6	336.12	136.69	0.23	9.91

*These data were not measured.

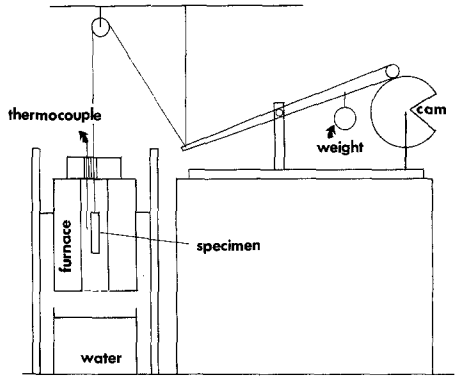

Figure 5 Schematic diagram of the thermal shock test apparatus including furnace and quenching bath.

3.2. Affects of cyclic thermal shock on elasticity and internal friction

Figs 6 to 8 display the effects of cyclic thermal shock on the Young's modulus, E, shear modulus, G, and internal friction, Q^{-1} for the unreinforced alumina specimens. At low and intermediate values of thermal shock severity, ΔT, the internal friction and modulus of the unreinforced alumina specimens behaved the same as the SiC whisker reinforced alumina [4, 5]. Decreases in both the Young's modulus and the shear modulus always accompanied an increase in internal friction (Figs 6 to 8). As ΔT increases, the thermal shock damage saturation levels also increase, as indicated by changes in modulus and internal friction.

Relative changes in modulus and internal friction are listed in Table IV for each of the six thermally shocked alumina specimens. The magnitude of the internal friction changes were much larger than modulus changes, which agrees with trends in elastic modulus and internal friction observed in other studies [4–6, 8, 9, 35].

For the unreinforced alumina specimens included in this study, no saturation behaviour was observed for

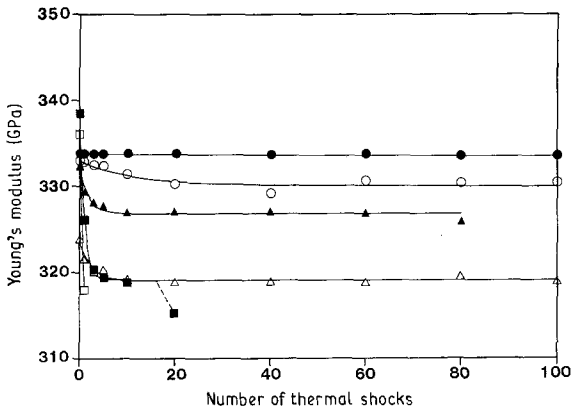

Figure 6 Young's modulus of alumina specimens, A1 (●, ΔT = 230° C), A2 (○, ΔT = 250° C), A3 (△, ΔT = 270° C), A4 (▲, ΔT = 290° C), A5 (■, ΔT = 310° C), and A6 (□, ΔT = 380° C) as a function of the cumulative number of thermal shock cycles. Full curves represent least-squares best fit to $E = E_0 - A[1 - \exp(-\alpha n)]$.

†In polymer composites, internal friction contributions due to matrix–fibre interactions have been observed [40]. Similar effects are likely in ceramic composites.

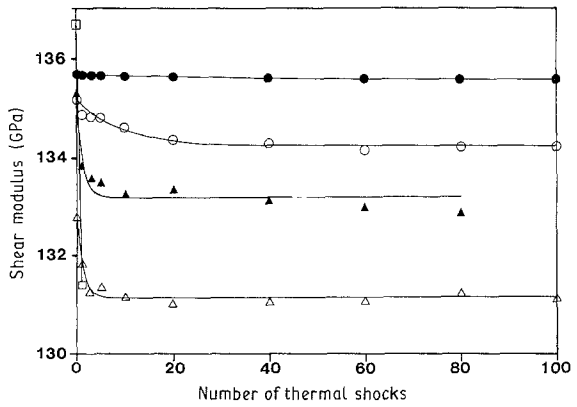

Figure 7 Shear modulus of alumina specimens, A1 (●, ΔT = 230° C), A2 (○, ΔT = 250° C), A3 (△, ΔT = 270° C), A4 (▲, ΔT = 290° C) and A6 (□, ΔT = 380° C) as a function of the cumulative number of thermal shock cycles. Full curves represent least squares best fit to $G = G_0 - C[1 - \exp(-\gamma n)]$.

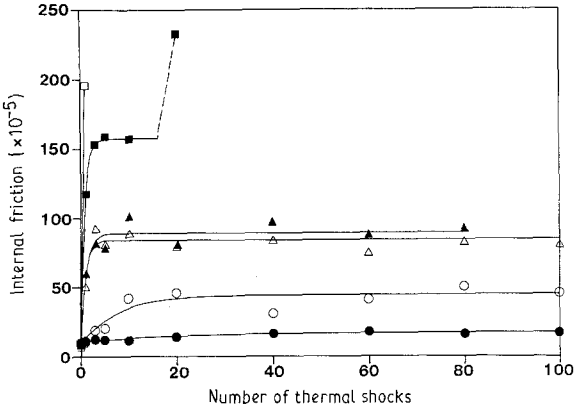

Figure 8 Internal friction of alumina specimens, A1 (●, ΔT = 230° C), A2 (○, ΔT = 250° C), A3 (△, ΔT = 270° C), A4 (▲, ΔT = 290° C), A5 (■, ΔT = 310° C), and A6 (□, ΔT = 380° C) as a function of the cumulative number of thermal shock cycles. Full curves represent least-squares best fit to $Q^{-1} = Q_0^{-1} + B[1 - \exp(-\beta n)]$.

the two most severe thermal shock conditions (ΔT = 310 and 380° C). Specimen A5 (ΔT = 310° C) apparently approached saturation in the interval between five and ten thermal shock cycles. An abrupt decrease in the Young's modulus and an abrupt increase in internal friction, however, occurred for specimen A5 in the interval between 11 and 20 thermal shock cycles. The abrupt change may result from the linkage of the microcracks to form macrocracks, since a corner of the specimen A5 broke off after 40 cumulative thermal shock cycles. The corner fragment had a mass of 0.083 g, compared to a total specimen mass of 5.815 g. For specimen A6 (ΔT = 380° C), thermal shock damage was measurable only after the first and second thermal shock cycle since the specimen broke into two large pieces as a result of the third thermal shock.

For a temperature difference of 290° C, specimen A4 showed damage saturation behaviour between 10 and 80 cumulative cycles. A 0.145 g fragment broke off from a corner of the specimen after 81 thermal shock cycles (total mass of A4 was 5.816 g). In Figs 6 to 8, note the slight changes from the saturation damage level that are evident in the modulus and internal friction measurements at the 80 cumulative cycles. The fracture of a portion of the specimen upon the 81st thermal shock cycle implies that the deviation from the saturation damage level may be related to microcrack link-up and the failure of a portion of the specimen.

In contrast to the unreinforced alumina composites, none of the SiC whisker reinforced alumina specimen exhibited macrofracture (none of the SiC whisker–alumina specimen fractured for temperature differences ΔT up to 380° C [5]). In addition, each of the SiC whisker–alumina specimens showed damage saturation behaviour for up to 100 cumulative thermal shock cycles [5].

3.3. Quantitative analysis of thermal shock damage

3.3.1. Modulus and internal friction as a function of repeated thermal shocks

The same empirical equations developed by the present authors for the modulus and internal friction changes of thermally shocked SiC whisker reinforced

TABLE IV Relative changes in modulus and internal friction for the thermally shocked unreinforced alumina specimens and SiC whisker reinforced alumina composites. The subscript "0" refers to the value of the indicated parameter prior to the initial thermal shock, while the subscript "sat" refers to the "saturated" or steady-state value of the parameter that is obtained after repeated thermal cycling (see Equations 4 to 8).

Specimen label	ΔT(° C)	$(E_0 - E_{sat})/E_0$	$(G_0 - G_{sat})/G_0$	$(Q_{sat}^{-1} - Q_0^{-1})/Q_0^{-1}$
Unreinforced polycrystalline alumina				
A1	230	0.0010	0.0009	0.56
A2	250	0.0078	0.0060	6.81
A3	270	0.0143	0.0122	9.00
A4	290	0.0171	0.0157	10.09
A5	310	0.0575	*	24.08
A6	380	†	†	†
SiC whisker reinforced alumina composites				
HP160	270	0.007	*	1.2
HP171	310	0.0172	*	3.18
HP160-RA	340	0.0285	*	5.04
HP158	380	0.0583	*	10.49

*Shear modulus was not measured for this specimen.
†For ΔT = 380° C, the specimen fractured after third thermal shock, so that saturation values of moduli and internal friction could not be determined.

alumina composites [5] can be fit to the thermal shock data for the unreinforced alumina, namely

$$E = E_0 - A[1 - \exp(-\alpha n)] \quad (4)$$

and

$$Q^{-1} = Q_0^{-1} + B[1 - \exp(-\beta n)] \quad (5)$$

where A and B are damage saturation parameters (see Fig. 9), α and β the rate of decrement or increment (rate constant), respectively, E_0, and Q_0^{-1} the undamaged specimen's Young's modulus or internal friction, respectively, E, and Q^{-1} the damaged specimen's Young's modulus or internal friction, respectively and n the cumulative number of thermal shock cycles at a fixed ΔT value.

For the shear modulus, we introduce the relationship

$$G = G_0 - C[1 - \exp(-\gamma n)] \quad (6)$$

where C is the damage saturation parameter (see Fig. 9), γ the rate of decrement (rate constant), G_0 the undamaged specimen's shear modulus and G the damaged specimen's shear modulus.

For a fixed value of ΔT, the constants A, B and C represent a damage saturation or steady state level of damage for a large number of thermal shock cycles (Fig. 9). The constants α, β and γ are related to the rate of change of the modulus or internal friction as a function of thermal cycle treatment. We see from Equations 4, 5 and 6 that in the limit of $n \to 0$, $dE/dn = -A\alpha$, $dG/dn = -C\gamma$, and $dQ^{-1}/dn = B\beta$.

Table V shows the results of the non-linear regression based on Equations 4, 5 and 6. As ΔT increases, the damage saturation, A, B and C increase, and the rate constants, α, β, and γ increase. As discussed previously, Equations 4 and 5 were used to describe the thermal fatigue behaviour in SiC whisker–alumina composites [5], but the authors found the same equations could describe the thermal fatigue behaviour of the unreinforced polycrystalline alumina. The parameters A, B, α and β for the SiC whisker–alumina were, however, different from the corresponding parameters for the unreinforced alumina. As discussed in Section 3.4, the damage for given values of ΔT and n is greater for the unreinforced alumina than for the SiC whisker–alumina composites.

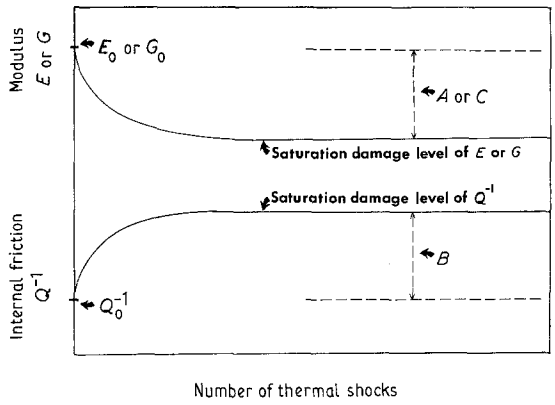

Figure 9 Schematic diagram illustrating thermal shock saturation levels A, B and C and the rate constants α, β and γ. (see Equations 4 to 6.)

3.3.2. Relation between Young's modulus saturation constant A and shear modulus saturation constant C

Equations 4 and 6, respectively, describe the decrease in Young's modulus and decrease in shear modulus with microcrack damage accumulation. For a sufficiently high number of thermal shock cycles, n, the factors $[1 - \exp(-\alpha n)]$ and $[1 - \exp(\gamma n)]$ approach unity and Equations 4 and 6 become

$$E_{sat} = E_0 - A \quad (7)$$

thus

$$E_{sat}/E_0 = 1 - A/E_0$$

$$G_{sat} = G_0 - C \quad (8)$$

TABLE V For the unreinforced alumina specimens, results of the non-linear regression analysis for the damage saturation parameters A, B, and C and the rate constants α, β and γ (see Equations 4 to 6 and Fig. 9). The unshocked values of internal friction Q_0^{-1}, Young's Modulus, E_0, and shear modulus, G_0, are included for reference.

Specimen	A1	A2	A3	A4	A5	A6
ΔT (°C)	230	250	270	290	310	380
Q_0^{-1} ($\times 10^{-5}$)	10.6	8.1	8.6	8.3	6.2	9.9
E_0 (GPa)	333.85	332.96	323.87	332.50	338.53	336.12
G_0 (GPa)	135.68	135.17	132.78	135.32	*	136.69
A (GPa)	0.34	2.87	4.77	5.70	19.42	†
B ($\times 10^{-5}$)	6.0	34.9	75.4	80.68	150.9	†
C (GPa)	0.12	0.95	1.64	2.13	*	†
α	0.030	0.087	0.499	0.616	1.005	†
β	0.050	0.145	0.970	0.927	1.338	†
γ	0.036	0.178	0.836	0.886	*	†
correlation coefficient (α, A)	0.96	0.92	0.97	0.96	0.99	†
correlation coefficient (β, B)	0.96	0.94	0.98	0.97	0.99	†
correlation coefficient (γ, C)	0.99	0.97	0.98	0.95	*	†

*Shear modulus was not measured for this specimen.
†At ΔT = 380°C, no saturation behaviour was observed since the specimen broke into two pieces after third thermal shock.

thus

$$G_{sat}/G = 1 - C/G_0$$

where E_{sat} and G_{sat} are the saturation (steady state) values of the moduli as a function of the cumulative number of thermal shock cycles (Figs 6 and 7).

Salganik's [42] relation for the decrement in Young's modulus, E, and shear modulus, G, are

$$E = E_0 (1 - f(\nu_0)\varepsilon) \quad (9)$$

$$G = G_0 (1 - g(\nu_0)\varepsilon) \quad (10)$$

where

$$f(\nu_0) = 16 (10 - 3\nu_0)(1 - \nu_0^2)/45(2 - \nu_0) \quad (11)$$

$$g(\nu_0) = 32(1 - \nu_0)(5 - \nu_0)/45(2 - \nu_0) \quad (12)$$

At the saturated state, Equations 9 and 10 can be rewritten as

$$E_{sat}/E_0 = 1 - f(\nu_0)\varepsilon_{sat} \quad (13)$$

$$G_{sat}/G_0 = 1 - g(\nu_0)\varepsilon_{sat} \quad (14)$$

where ε_{sat} is the crack damage parameter at the saturated microcrack damage state. Combining Equations 7 and 13 gives

$$A/E_0 = f(\nu_0)\varepsilon_{sat} \quad (15)$$

Likewise, Equations 8 and 14 yield

$$C/G_0 = g(\nu_0)\varepsilon_{sat} \quad (16)$$

Combining Equations 15 and 16 gives

$$C = [g(\nu_0)/f(\nu_0)](G_0/E_0)A \quad (17)$$

The relation between Young's modulus and shear modulus is given by

$$G_0 = E_0/2(1 + \nu_0) \quad (18)$$

Substituting G_0/E_0 from Equation 18 into Equation 17 yields

$$C = k(\nu_0)A \quad (19)$$

where

$$k(\nu_0) = [(5 - \nu_0)/(10 - 3\nu_0)(1 + \nu_0)^2] \quad (20)$$

The proportionality constant $k(\nu_0) = 0.34$ for the alumina specimens included in this study (where Poisson's ratio ranged from 0.22 to 0.23). A least squares best fit of the experimental data for C against A yielded an experimental value of 0.357 for $k(\nu_0)$, with a correlation coefficient of 0.98 (Fig. 10). Thus based on Salganik's theoretical results, Equation 19, which has no free parameter, predicts well the observed linear relation between the elastic modulus damage parameters A and C. If Poisson's ratio, ν_0, and the damage parameter, A, are known then the damage parameter, C can be predicted from Equations 19 and 20.

3.3.3. ΔQ^{-1} as a function of crack density parameter, ε

From Salganik's Equation 9 and empirical Equations 4 and 5, the internal friction change can be expressed as [4, 5]

$$\Delta Q^{-1} = C_1[1 - (1 - C_2\varepsilon)^{C_3}] \quad (21)$$

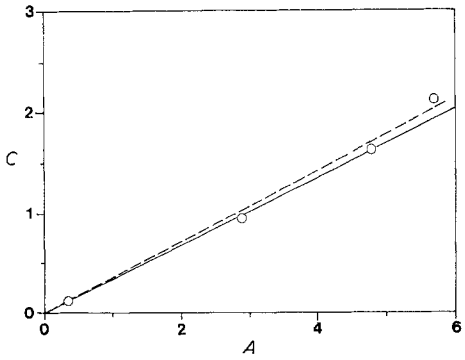

Figure 10 Relation between the measured elastic moduli damage saturation parameters, A and C. The broken line corresponds to the least squares fit to the experimental data, while the full curve is the relation predicted from Equations 19 and 20 (using the measured values of Poisson's ratio to determine the proportionality constant $k(\nu_0)$.

where C_1, C_2 and C_3 are constants. For a sufficiently small $C_2\varepsilon$, the term $(1 - C_2\varepsilon)^{C_3}$ in Equation 21 can be written as $(1 - C_1C_2\varepsilon)$ using the binomial expansion therorem. The Equation 21 can be approximated to linear equation, $\Delta Q^{-1} = D\varepsilon$, where D is constant.

A least-square best fit of Equation 21 yields 19.44×10^{-5}, 670, and 0.64 for C_1, C_2, and C_3, respectively. In the previous study, the value C_2 of the alumina–SiC composites [5] was 390, which is relatively small and the linear approximation to the power-law form is in fact a good approximation. The C_2 value of the present study is, however, relatively higher than that of the previous study, the linear approximation to the power-law form is not so good as compared to the previous study, (Fig. 11). In Fig. 11 the five ΔQ^{-1} and ΔE against ε curves in Figs 6 and 8 are effectively collapsed onto a single line of ΔQ^{-1} against ε, crack damage parameter.

3.3.4. The dependence of the damage saturation parameters on the thermal shock temperature difference

The normalized saturation values, A/E_0, C/G_0 and B/Q_0^{-1} show a power law relationship with

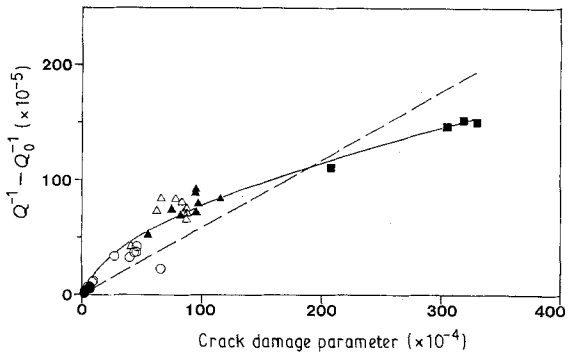

Figure 11 ΔQ^{-1} as a function of ε for the alumina specimens. Symbols indicate the ΔT value for a given measurement on thermally fatigued specimens. Symbols are the same in Figs 6 and 7 (●, ΔT = 230° C; ○, ΔT = 250° C; ▲, ΔT = 270° C; △, ΔT = 290° C; ■, ΔT = 310° C; □, ΔT = 380° C). Note that measurements with similar ΔT values are grouped together along the curve. Full curve represents least-squares best fit to power law relation. Broken curve represents best fit to linear equation in ε.

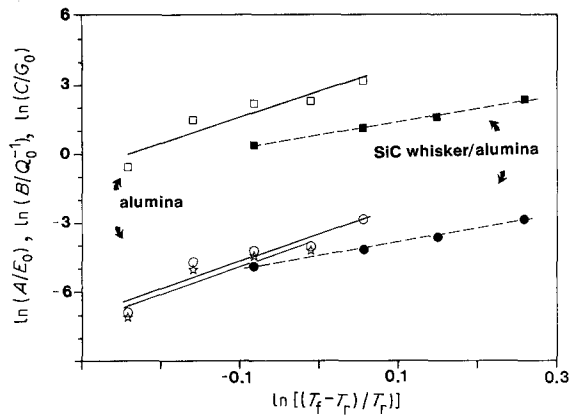

Figure 12 Logarithm of the normalized saturation damage parameters (A/E_0) and (B/Q_0^{-1}) against logarithm of the normalized temperature. (□ ■ ln (B/Q_0), ○ ● ln (A/E_0), ☆ ln (C/G_0).)

non-dimensional temperature difference, $\Delta T/T_r$, (Fig. 12) namely

$$A/E_0 = j1(\Delta T/T_r)^{p^1} \quad (22)$$

$$B/Q_0^{-1} = j2(\Delta T/T_r)^{p^2} \quad (23)$$

$$C/G_0 = j3(\Delta T/T_r)^{p^3} \quad (24)$$

where T_r, a reference temperature, was taken as 293 K (room temperature). ΔT, the temperature difference between the furnace temperature and the water bath temperature, was expressed in Kelvin. A least-squares best fit yielded $j1 = 0.030, j2 = 14.79$ and $j3 = 0.026$ for Equations 22, 23 and 24. The exponents p^1, p^2 and p^3 are, respectively, 11.8, 11.3 and 12.1.

Fig. 12 compares the temperature dependence of the saturation damage levels for the unreinforced alumina (plotted using the open symbols) and the SiC whisker reinforced alumina (the closed symbols). In this log–log plot, the slopes of the curves correspond to p^1, p^2, and p^3 in Equations 22 to 24. Slopes of ln (A/E_0) and ln (B/Q_0^{-1}) against ln ($\Delta T/T_r$) are very similar for the SiC whisker reinforced alumina (5.9 and 5.7 respectively). Similarly, the slopes of ln (A/E_0), ln (B/Q_0^{-1}), and ln (C/G_0) are very similar for the unreinforced alumina (11.8, 11.3, and 12.1, respectively). For both the composite and non-composite specimens, the thermal shock damage level as measured by either the elastic modulus or by internal friction, has a very similar functional dependence on the quenching temperature difference.

The exponents p^1 and p^2 of the polycrystalline alumina are almost double those of the SiC whisker reinforced alumina composites. From Equation 22 and 23, we see that doubling the exponents p^1 and p^2 squares the value of A and B. Thus the polycrystalline alumina specimens are far more sensitive to thermal shock damage as a function of ΔT than are the SiC whisker reinforced alumina composites, therefore, the whisker reinforcement is shown to dramatically improve the thermal shock damage of alumina.

As observed in previous studies [4, 5], the relative changes in internal friction are much larger than the corresponding changes in elastic modulus, for a given level of thermal shock damage. For a given ΔT, and for a fixed reference temperature T_r, the ratio of the two normalized saturation parameters (B/Q_0^{-1})/(A/E_0) is approximately equal to $j2/j1$ (see Equations 22 and 23). The ratio $j2/j1$ (which is approximately 500) is a "sensitivity ratio" [5] since it represents, for a given level of thermal shock damage, the relative sensitivity (or relative change) in internal friction compared to the changes observed for Young's modulus. In comparison, the sensitivity ratio for the SiC whisker reinforced alumina composites was about 200 [5].

The sensitivity ratio $j3/j1$ is (C/G_0)/(A/E_0) for a given ΔT represents a relative sensitivity in shear modulus compared to the changes observed for Young's modulus. Thus the saturation damage C can be expressed as

$$C = (G_0/E_0)(j3/j1)A \quad (25)$$

where for the unreinforced alumina $G_0/E_0 = 1/2(1 + \nu_0)$ has the value of 0.41 and $j3/j1 = 0.88$. Thus Equation 25 becomes $C = 0.36A$, which is essentially identical to the numerical results obtained in a different manner from Equation 19 (Section 3.3.2.).

In Equations 22 to 24, the power law in ΔT can be replaced by a power law in thermal stress, since the thermal shock induced stresses are linearly proportional to the temperature difference. Also the saturation damage parameters can be expressed in terms of integrated crack growth [5]. Thus, Equations 22 to 24 can be expressed as a power law function of stress intensity factor, K [5]. This power law relation in stress intensity factor, K shows a fatigue relationship similar to that of metals.

3.4. Comparison of the cyclic thermal shocks in unreinforced alumina and SiC whisker reinforced alumina composites

Water quenching of samples produces time varying tensile stresses at surface regions of the specimen. For simple geometry (a flat plate, for example), the maximum stresses can be evaluated using an equation such as [43]

$$\sigma_{max} = f(N_{bi})[E\alpha\Delta T/(1 - \nu)] \quad (26)$$

where σ_{max} is the maximum value of the actual surface stress, E the Young's modulus, α the average thermal expansion coefficient, ΔT the temperature difference of thermal shock, ν Poisson's ratio and $f(N_{bi})$ the function of Biot number (maximum non-dimensional thermal stresses at the surface). The Biot number, N_{bi}, is a non-dimensional parameter given by

$$N_{bi} = ht/k \quad (27)$$

where h is the heat transfer coefficient, t the half thickness of plate and k the thermal conductivity.

Manson [44] described $f(N_{bi})$, the maximum non-dimensional thermal stresses at the surface of the plate, as

$$f(N_{bi}) = 1/[1.5 + 3.25/N_{bi}] \quad (28)$$

for $0 < N_{bi} < 5$. The N_{bi} values for the unreinforced polycrystalline alumina and SiC whisker reinforced alumina listed in Table VI satisfy the assumption to use Equation 28, thus we can use Equation 26 to compare the magnitudes of the maximum non-dimensional surface thermal stresses for the

TABLE VI Thermal properties of polycrystalline alumina and SiC whisker reinforced alumina including the heat transfer coefficient, h, the thermal conductivity, k, and the Biot modulus, N_{bi}.

	h (cal sec^{-1} cm^{-2} °C^{-1}) (for water quenching)	t (cm)	k (cal sec^{-1} cm^{-1} °C^{-1})	N_{bi}*
Polycrystalline Alumina	0.1–1.0 [45]	0.05	0.077 [46]	0.07–0.65
SiC Whisker Reinforced Alumina	0.1–1.0 [45]	0.15	0.084 [46]†	0.18–1.79

*N_{bi} is calculated from Equation 27.
†There was 20 vol % of SiC whisker in the alumina matrix both in this study and [46].

unreinforced alumina and for SiC whisker reinforced alumina composites [5]. To simplify the calculations, we shall assume the same range for the heat transfer coefficient, h, for both the unreinforced alumina and SiC whisker reinforced alumina composites (Table VI). According to Equation 26, the maximum thermally induced stresses for alumina–SiC whisker composites were two to three times larger than those for the unreinforced alumina specimens largely because the alumina specimens used in this research were thinner than the alumina–SiC whisker composites used in the earlier study [5].* (The thicker specimens have corresponding higher values of N_{bi}, as shown in Equation 27.) Nevertheless, the damage (as determined by elasticity and internal friction measurements) in the unreinforced alumina specimens was much larger than the thermal shock induced in the alumina–SiC whisker composites (Table VII). For example, the relative changes in Young's modulus and internal friction for the unreinforced alumina at $\Delta T = 270°$ C were 1.4 and 900% respectively. In contrast, the Young's modulus and internal friction changes for alumina–SiC whisker composites at the same ΔT were 0.7 and 120%. The rate constant and the saturation value of alumina–SiC composites are much smaller than those of unreinforced alumina, (Table VII) which indicates that the thermal shock resistance of the SiC whisker reinforced alumina composites is superior to the unreinforced polycrystalline alumina.

4. Conclusions

The accumulation of thermal shock induced microcrack damage for thermally cycled alumina was monitored by modulus and internal friction changes. For low and intermediate values of ΔT (thermal shock severity) the thermal shock damage tends to saturate at a sufficiently high number of thermal cycles. This saturation value increases as thermal shock temperature difference increases.

The relative change in internal friction plotted against the damage parameter ε can be expressed as a power law relation for each of the five thermally shocked specimens. The five Q^{-1} against n curves in Fig. 8 are replotted in Fig. 11 in terms of ΔQ^{-1} against ε damage parameter. The five† internal friction curves from Fig. 8 thus collapse onto a single curve plot of ΔQ^{-1} against ε. Thus the thermal shock damage, at least for the specimens included in this study, can be expressed as a power law function of the crack damage parameter.

A power law relationship between the saturation damage level and thermal shock difference implies a fatigue-like power law relation in stress. The crack growth rates for the polycrystalline specimens are far more sensitive to ΔT than SiC whisker reinforced alumina composites. The exponent in the power law was determined to be about 12 for the unreinforced polycrystalline alumina (about 2 times larger than that of SiC whisker reinforced alumina composites).

Acknowledgements

The authors would like to acknowledge the financial support of the National Science Foundation under Grant number MSM-8706915. The authors also would like to acknowledge Saxonburg Ceramic Incorporated, Monroe, North Carolina for providing the polycrystalline alumina.

TABLE VII Comparison of damage saturation values A and B, rate constants α and β, and relative changes in Young's modulus and internal friction for unreinforced alumina and alumina–SiC whisker composites [5].

ΔT	Material	A (GPa)	B ($\times 10^{-5}$)	α	β	A/E_0	B/Q_0^{-1}
270	alumina–SiC composite	3.00	20.38	0.042	0.061	0.007	1.2
	unreinforced alumina	4.77	75.44	0.499	0.970	0.0143	9.0
310	alumina–SiC composite	6.21	33.65	0.220	0.105	0.0172	3.18
	unreinforced alumina	19.42	150.88	1.005	1.338	0.0575	24.08

*The dimensions for the unreinforced alumina were 11.5 × 1.3 × 0.1 cm^3, whereas the dimensions for the SiC whisker reinforced alumina composites were 7 × 0.7 × 0.3 cm^3.
†The data for the specimen A6 was not included in this figure, since saturation behaviour was not observed for the specimen A6.

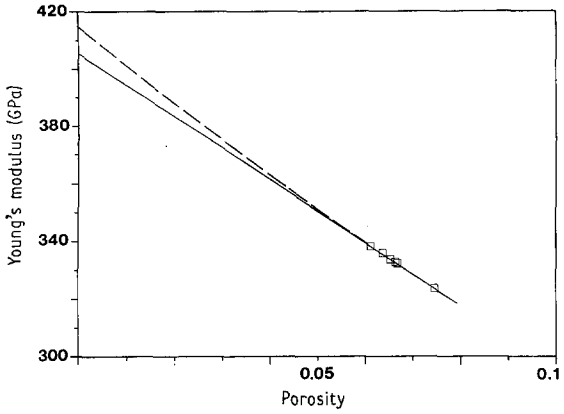

Figure A1 Young's modulus of the alumina as a function of porosity prior to thermal shock damage. Full curve represents least-squares best fit to linear equation. Broken curve represents least-squares best fit to exponential relation.

Appendix A. Moduli and internal friction as a function of porosity

Generally, the modulus decreases and internal friction increases as the porosity increases. In this study, the volume fraction porosity, P, of the polycrystalline alumina specimens ranged from 0.061 to 0.074. The measured elastic modulus for each of the undamaged polycrystalline alumina specimen used in this study are not identical because of the porosity differences among the specimens. In this appendix, we show that these differences can be expanded in terms of well-known functional forms for modulus–porosity relations. Using these modulus–porosity relations, we extrapolate to zero porosity and find that the unshocked, zero porosity extrapolations of modulus agree well with the elastic moduli calculated from single crystal data.

Modulus–porosity relations for these alumina specimens were adequately represented by the following semi-empirical exponential forms

$$E = E_0 \exp(-aP) \quad \text{(A1)}$$

$$G = G_0 \exp(-bP) \quad \text{(A2)}$$

where E_0, and G_0 are the Young's modulus and shear modulus, respectively, of non-microcracked, theoretically dense alumina, P the volume fraction porosity and a and b empirical constants. For small P values,

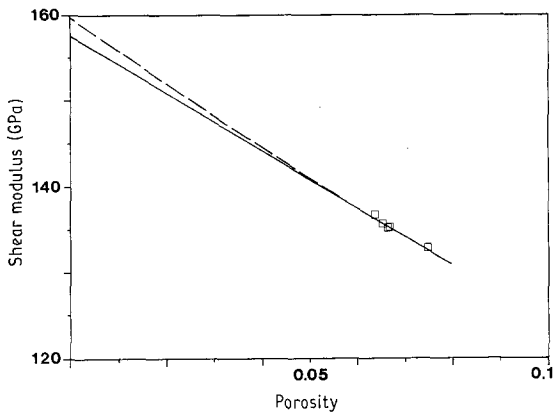

Figure A2 Shear modulus of the alumina as a function of porosity prior to thermal shock damage. Full curve represents least-squares best fit to linear equation. Broken curve represents least-squares best fit to exponential relation.

TABLE AI Results of least squares best fit to porosity–modulus equation.

	Exponential equation	Linear equation
E_0 (GPa)	414.41	405.36
Constant a, c	3.34	2.70
Correlation coefficient	0.99	0.99
G_0 (GPa)	159.67	157.59
Constant b, d	2.48	2.12
Correlation coefficient	0.97	0.98
ν_0	0.229	0.222

the empirical exponential equations can be approximated by linear functions, which are

$$E/E_0 = 1 - cP \quad \text{(A3)}$$

$$G/G_0 = 1 - dP \quad \text{(A4)}$$

where c and d are the porosity–modulus slope.

The results of least-squares best fit to Equations A1 to A4 are listed in Table AI and shown in Figs A1 and A2. In all cases, the correlation coefficients are greater than 0.97.

The expected bounds for the Young's modulus and shear modulus of a theoretically dense polycrystalline bodies can be calculated from the elasticity data of that single crystal. The Voigt and Reuss bounds calculated from measurements on single crystal alumina [47] (Table AII) are upper and lower bounds of the theoretically dense materials' elastic constants. Since these bounds are calculated from single crystal data, these aggregate bounds may be used to estimate the elastic moduli of theoretically dense polycrystalline specimens. The least-square best fit to the exponential equations A1 and A2 differs by 2.7 and 2.2% with the E_0 and G_0 obtained from the mean of Voigt and Reuss bounds (Tables AI and AII). In contrast, the least-square best fit to the linear Equations A3 and A4 yields $E_0 = 405.36$ GPa and $G_0 = 157.59$ GPa, which differs by 0.5 and 3.4% with the E_0 and G_0 from mean of Voigt and Reuss bounds (Tables AI and AII).

In the present study, the internal friction of the alumina specimens did not show a dependence on porosity (Fig. A3) for the restricted range of porosity exhibited by the specimens in this study.

In studies of polycrystalline yttria [48] and magnesia [49], Marlowe [48] and Hanna *et al.* [49] fit their internal friction data to a power function of porosity, P, such as

$$Q^{-1} = FP^r \quad \text{(A5)}$$

where F, r = empirical constant.

TABLE AII The Voigt and Reuss bounds calculated from measurements on single crystal alumina [47] along with the arithmatic mean of those bounds for the elastic moduli.

Bound type	Young's modulus (GPa)	Shear modulus (GPa)	Poisson's ratio
Voigt	408.5	165.7	0.223
Reuss	398.3	160.7	0.239
Mean	403.4	163.2	0.236

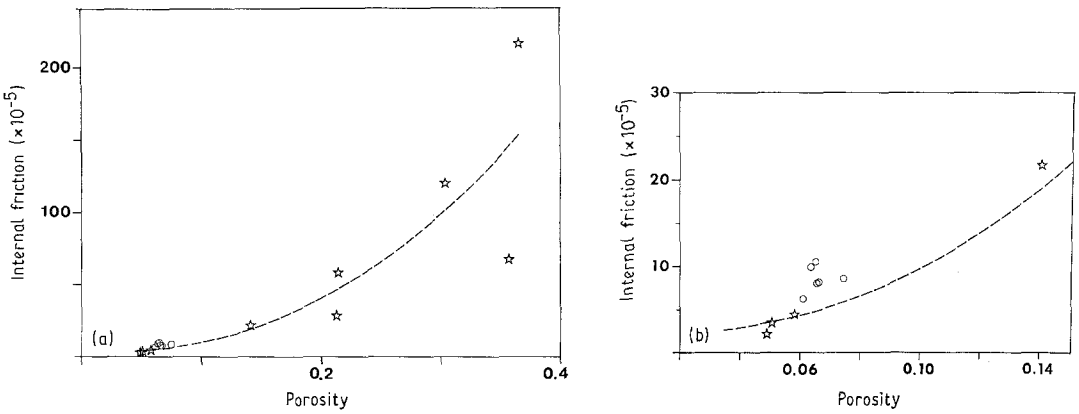

Figure A3 Internal friction of the Y_2O_3 as a function of porosity (after Marlowe [48]). (☆ yttria (after Marlowe), ○ alumina (present-study). Broken curve represents least-squares best fit to power law relation.

For Marlowe's data on polycrystalline yttria, F and r are 0.009 and 1.925, respectively. For a zero value of porosity, Q^{-1} will not, however, be zero, as predicted by Equation A5. There are a number of physical mechanisms other than porosity that contribute to internal friction [50, 51]. Thus Equation A5 should be modified as follows

$$Q^{-1} = Q_0^{-1} + F'P^{r'} \quad \text{(A6)}$$

where Q_0^{-1} is the zero porosity internal friction and $F'$and r' are empirical constants.

Fig. A3 shows a least-squares best fit of revised Equation A6 to Marlowe's internal friction data. In the present study, the porosity range was so narrow (6.1 to 7.5%) that the affect of porosity on internal friction cannot be monitored (Fig. A3).

References

1. M. ASHIZUKA, T. E. EASLER and R. C. BRADT, *J. Amer. Ceram. Soc.* **66** (1983) 542.
2. W. P. ROGERS, A. F. EMERY, R. C. BRADT and A. S. KOBAYASHI, *ibid.* **70** (1987) 406.
3. H. OHIRA and R. C. BRADT, *ibid.* **71** (1988) 35.
4. W. J. LEE, MS Thesis, Michigan State University, East Lansing, Michigan (1988).
5. W. J. LEE and E. D. CASE, *Mater. Sci. Eng.* **A119** (1989) 113.
6. H. M. CHOU, PhD Dissertation, Michigan State University, East Lansing, Michigan (1988).
7. C. E. SEMLER, Jr., T. H. HAWISHER and R. C. BRADT, *Amer. Ceram. Soc. Bull.* **60** (1981) 724.
8. K. MATSUSHIDA, S. KURATANI, T. OKAMOTO and M. SHIMADA, *J. Mater. Sci. Lett.* **3** (1984) 345.
9. J. C. COPPOLA and R. C. BRADT, *J. Amer. Ceram. Soc.* **56** (1973) 214.
10. M. J. REECE, F. GUIU and M. F. R. SAMMUR, *ibid.* **72** (1989) 348.
11. T. HOSHIDE, T. OHARA and T. YAMADA, *Int. J. Frac.* **37** (1988) 47.
12. A. GROSSMULLER, V. ZELIZKO and M. V. SWAIN, *J. Mater. Sci. Lett.* **8** (1989) 29.
13. R. H. DAUSKARDT, W. YU and R. O. RITCHIE, *J. Amer. Ceram. Soc.* **70** (1987) C-248-C-252.
14. K. KIM and A. MUBEEN, STP 745 (American Society for Testing and Materials, Philadelphia, 1981) pp. 157–168.
15. R. W. HERTZBERG, "Deformation and Fracture Mechanics of Engineering Materials" 2nd edn. (John Wiley, New York, 1983) pp. 521–523.
16. A. G. EVANS and R. M. CANNON, *Acta Metall.* **34** (1986) 761.
17. D. B. MARSHALL, M. D. DRORY and A. G. EVANS, in "Fracture Mechanics of Ceramics", Vol. 6, edited by R. C. Bradt, A. G. Evans, D. P. H. Hasselman and F. F. Lange (Plenum Press, New York, 1983) pp. 289–307.
18. K. T. FABER and A. G. EVANS, *Acta Metall.* **31** (1983) 565.
19. *Idem, ibid.* **31** (1983) 577–584.
20. P. L. SWANSON, C. J. FAIRBANKS, B. R. LAWN, Y-M. MAI and B. J. HOCKEY, *J. Amer. Ceram. Soc.* **70** (1987) 279.
21. J. R. BROCKENBROUGH and S. SURESH, *J. Mech. Phys. Solids* **35** (1987) 721.
22. L. EWART and S. SURESH, *J. Mater. Sci. Lett.* **5** (1986) 774.
23. L. EWART and S. SURESH, *J. Mater. Sci.* **22** (1987) 1173.
24. E. K. TSCHEGG and S. SURESH, *ibid.* **22** (1987) 2927.
25. S. SURESH and L. X. HAN, *J. Amer. Ceram. Soc.* **71** (1988) C-158-C-161.
26. A. A. MORRONE, S. R. NUTT and S. SURESH, *J. Mater. Sci.* **23** (1988) 3206.
27. S. SURESH and L. A. SYLVA, *Mater. Sci. Eng.* **83** (1986) L7.
28. F. A. McCLINTOCK and J. B. WALSH, in Proceedings of 4th US National Congress on Applied Mechanics (American Society of Mechanical Engineers, New York, 1962) pp. 1015.
29. V. TVERGAARD and J. W. HUTCHINSON, *J. Amer. Ceram. Soc.* **71** (1988) 157.
30. R. L. FULLMAN, *AIME* **197** (1953) 447.
31. F. FORSTER, *Z. Metallkunde* **29** (1937) 109.
32. G. PICKETT, *ASTM Proc.* **45** (1945) 846.
33. D. P. H. HASSELMAN, "Tables for Computation of Shear Modulus and Young's Modulus of Elasticity from Resonant Frequencies of Rectangular Prisms", (Carborundum Co., Niagara Falls, New York, 1961).
34. J. B. WACHTMAN, Jr. and W. E. TEFFT, *Rev. Sci. Instrum.* **29** (1958) 517.
35. S. L. DOLE, O. HUNTER, Jr. and C. J. WOOGE, *J. Amer. Ceram. Soc.* **60** (1977) 488.
36. D. F. PORTER, J. S. REED and D. LEWIS III, *ibid.* **60** (1977) 345.
37. S. L. DOLE, O. HUNTER, Jr. and F. W. CALDERWOOD, *ibid.* **60** (1977) 167.
38. B. R. POWELL, Jr., O. HUNTER, Jr., and W. R. MANNING, *ibid.* **54** (1971) 488.
39. V. D. KRSTIC and W. H. ERICKSON, *J. Mater. Sci.* **22** (1987) 2881.
40. D. CAWLEY and R. D. ADAMS, in "Non-Destructive Testing of Fiber Reinforced Plastic Composites", Vol. 1, edited by J. Summerscales (Elsevier Applied Science, New York, 1987) pp. 151–200.
41. E. D. CASE, J. R. SMYTH and O. HUNTER, Jr., in "Fracture Mechanics of Ceramics", Vol. 5, edited by R. C. Bradt, A. G. Evans, D. P. H. Hasselman and F. F. Lange (Plenum Press, New York, 1983) pp. 507–530.
42. R. L. SALGANIK, *Mech. Solids* **8** (1973) 135.

43. P. F. BECHER, D. LEWIS, K. R. CARMAN and A. C. GONZALEZ, *Bull. Amer. Ceram. Soc.* **59** (1980) S42.
44. S. S. MANSON, "Behaviour of Materials under Conditions of Thermal Stress", Technical Note 2933, National Advisory Committee for Aeronautics (Lewis Flight Propulsion Laboratory, Cleveland, Ohio, 1953) p. 103.
45. W. D. KINGERY, H. K. BOWEN and D. R. UHLMANN, in "Introduction to Ceramics" 2nd edn. (John Wiley, New York, 1976) Chaps 12 and 16.
46. T. N. TIEGS and P. F. BECHER, *J. Amer. Ceram. Soc.* **70** (1987) C-109-C-111.
47. G. SIMMONS and H. WANG, "Single Crystal Elastic Constants and Calculated Aggregate Properties: A Handbook" (MIT Press, Cambridge, MA, 1971).
48. M. O. MARLOWE, MS Thesis, Iowa State University, Ames, Iowa (1963).
49. R. HANNA and W. B. CRANDALL, "The Young's Modulus and Internal Friction of Polycrystalline MgO at Room Temperature", U.S. Atomic Energy Commission Report AROD-2891.1 (Army Research Office, Durham, North Carolina, 1961).
50. C. ZENER, "Elasticity and Anelasticity of Metals" (University of Chicago Press, Chicago, 1948).
51. T. S. KE, *Phys. Rev.* **74** (1948) 914.

Received 13 July
and accepted 1 November 1989